Supplementary Material

Accurately regulating the Ni coordination environment via atomic layer deposition and enabling the efficient CO_2 electroreduction

Xian Liu [a†], Shuangfeng Xing [c,d†], Jijie Li [b], Wen-Yan Zan [b], Zhe Gao [c,*] and Fengwei Zhang [b,*]

[a] College of Chemistry and Materials, Taiyuan Normal University, Jinzhong, 030619, P. R. China

[b] Institute of Crystalline Materials, Shanxi University, Taiyuan 030006, P. R. China

[c] State Key Laboratory of Coal Conversion, Institute of Coal Chemistry, Chinese Academy of Sciences, Taiyuan 030001, P. R. China

[d] School of Basic Medical Sciences, Hebei University, Baoding, 071002, P. R. China

***Corresponding Authors.** E-mail: gaozhe@sxicc.ac.cn; fwzhang@sxu.edu.cn

Electrochemical measurements

All electrochemical experiments were performed using a CS2350M electrochemical workstation under ambient temperature and pressure. The counter electrode (CE) was constructed using a platinum sheet, while the reference electrode (RE) comprised a saturated Ag/AgCl electrode. In the H-type cell, 0.5 M $KHCO_3$ was used as both the cathode and anode electrolytes, separated by a proton exchange membrane (Nafion 117), while the flow cell employed 1 M KOH for both electrodes, separated by an anion exchange membrane. All potential values are modified to RHE based on Nernst equation:

$$E_{RHE} = E_{measured} + E^{\theta}{}_{Ag/AgCl}\left(0.197\ V\right) + 0.0591 \times pH$$

Prior to conducting the electrochemical tests, CO_2 was introduced at a flow rate of 40 sccm for more than 30 min. Subsequently, a 30-minute constant-potential electrolysis experiment was conducted at each specified potential, with the CO_2 flow rate maintained at 20 sccm. The gaseous products were captured using an air bag, and their composition was assessed with the gas chromatography (GC) system (HXSP GC-950), which features a thermal conductivity detector (TCD) and two flame ionization detectors (FID), employing N_2 as the carrier gas and He as the internal standard. Under identical conditions, 1 mL of the gaseous sample from the air bag (approximately 200 mL in volume) was injected into the GC system using a sample lock syringe. The molar fractions of gaseous components in the injected samples were determined using gas chromatographic calibration curves. After each electrolysis, the extracted liquid product was quantified through ^1H NMR spectroscopy. The electrochemically active surface area (ECSA) was determined from the double-layer capacitance (C_{dl}), measured

via cyclic voltammetry within a potential range of −0.05 to 0.05 V *vs.* open circuit potential (OCP). To evaluate the long-term stability of 5Ni@NC-400H, continuous electrolysis was conducted over a duration of 60 h, with samples collected at hourly intervals. *In-situ* attenuated total reflection surface-enhanced infrared absorption spectroscopy (ATR-SEIRAS) measurements were conducted using a Nicolet iS50 FTIR spectrometer, operating in the spectral range of 800-4000 cm^{-1}. The catalyst was deposited on the Au- coated Si wafer substrate, with infrared spectra collected under applied potentials ranging from −0.2 V to −1.2 V *vs.* RHE. A background reference spectrum was recorded at the open circuit potential (OCP) prior to potential-controlled measurements.

The Faradaic efficiency (FE) and partial current density (*j*) for the gas products were calculated as the formulas:

$$FE = C \times S \times \left(ZFP / RT\right) / I_{total}$$

$$j = C \times S \times \left(ZFP / RT\right) / A$$

where *C* denotes the gas concentration measured by GC, *S* represents the CO_2 flow rate (20 sccm), *Z* is the electron transfer number for both CO and H_2 products (each with a value of 2), *F*, *P*, *R* and *T* represent the Faraday constant (96485 $C \cdot mol^{-1}$), the standard atmospheric pressure (101.325 kPa), the gas constant (8.314 $J \cdot mol^{-1} \cdot K^{-1}$) and the thermodynamic temperature (298.15 K), respectively. I_{total} refers to the current measured by the electrochemical workstation, and *A* is the area of the working electrode.

The turnover frequency (TOF) for CO_2RR-to-CO is determined using the following

equation:

$$TOF\ \left(s^{-1}\right) = \left[\left(j_{CO} \times A / ZF\right) / \left(m_{cat.} \times w / M_{Ni}\right)\right]$$

where j_{CO} refers to CO partial current density, $m_{cat.}$ denotes the mass of catalyst loading on the working electrode, M_{Ni} is the atomic mass of Ni, and w is the Ni content in the catalyst measured by ICP-MS.

Tafel slope was calculated by the following formula:

$$\eta = a + b \times \log(|j_{CO}|)$$

where η represents the overpotential, a is a constant influenced by the electrode material and solution composition, and b refers to the Tafel slope.

Theoretical calculations

DFT calculations were conducted utilizing the Vienna Ab-initio Simulation Package (VASP). The Perdew-Burke-Ernzerhof (PBE) functional was employed for exchange-correlation, and a plane-wave cutoff energy of 500 eV was adopted.[1-4] The 1Ni@NC-400H and 5Ni@NC-400H were selected as our models, and the free energy changes of the catalytic reactions were calculated using the computational hydrogen electrode (CHE) model. [5] The CO_2RR mechanism for generating CO involves two proton-coupled electron transfers: the initial step forms the *COOH intermediate, followed by the generation of the *CO intermediate, which subsequently desorbs.[6] The reaction steps are as below:

$$^* + CO_2(g) + H^+ + e^- \rightarrow {}^*COOH$$

$$^*COOH + H^+ + e^- \rightarrow {}^*CO + H_2O$$

$$^*CO \rightarrow {}^* + CO\ (g)$$

where * refers to the active site on the catalysts. The solvent effect of *COOH and *CO were considered and stabilized 0.25 and 0.10 eV, respectively.[7]

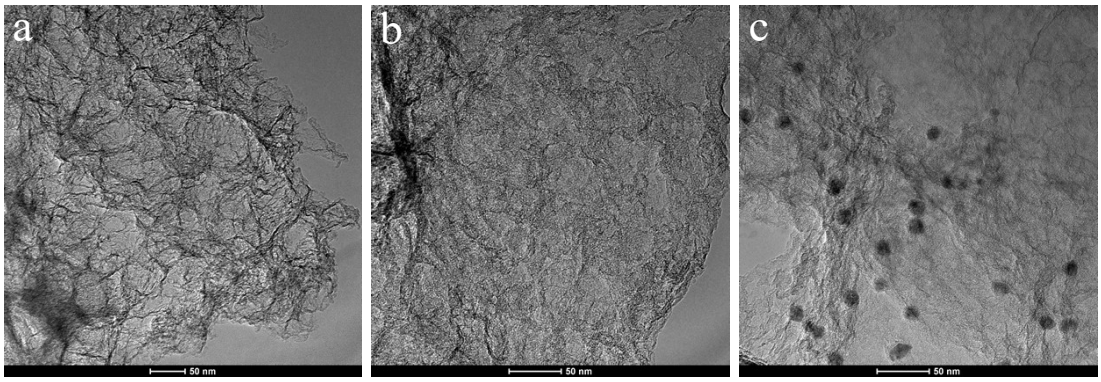

Fig. S1. TEM images of (a) 1Ni@NC-400H, (b) 5Ni@NC-400H and (c) 50Ni@NC-400H.

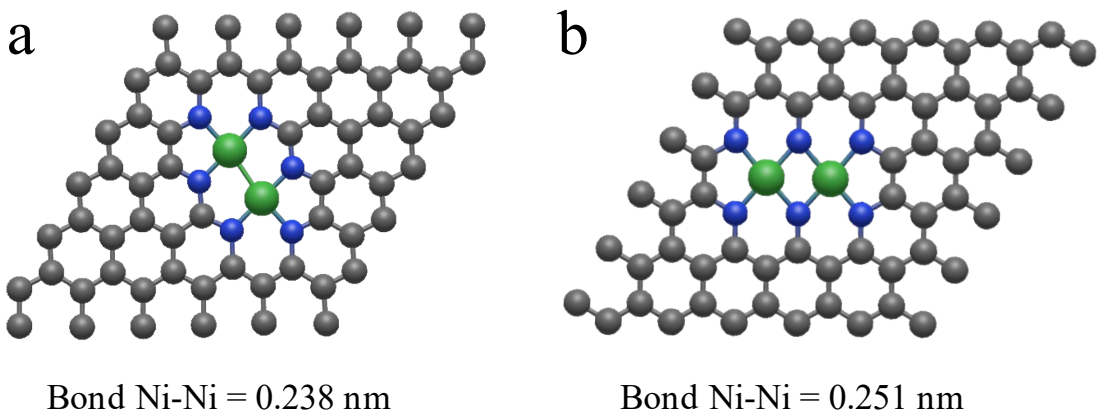

Fig. S2. Theoretical models of Ni dual-atomic site in N-doped carbon, along with the Ni atomic distance for (a) dual Ni-N_3 and (b) dual Ni-N_4.

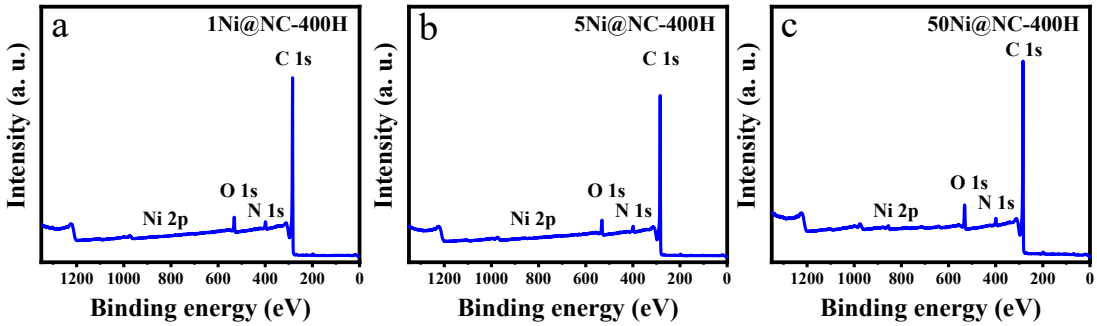

Fig. S3. XPS survey scans of (a) 1Ni@NC-400H, (b) 5Ni@NC-400H and (c) 50Ni@NC-400H catalysts.

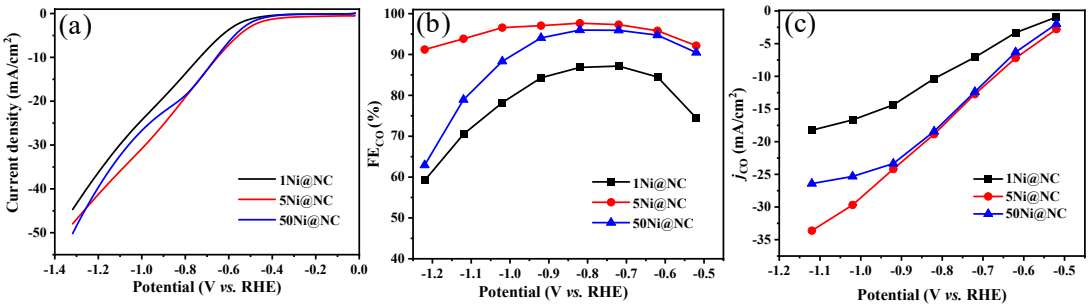

Fig. S4. (a) LSV curves, (b) FE_{CO}, FE_{H2} and (c) j_{CO} at various potentials over xNi@NC catalysts (before 400 °C H_2 treatment) in H-type cell (x = 1, 5 and 50).

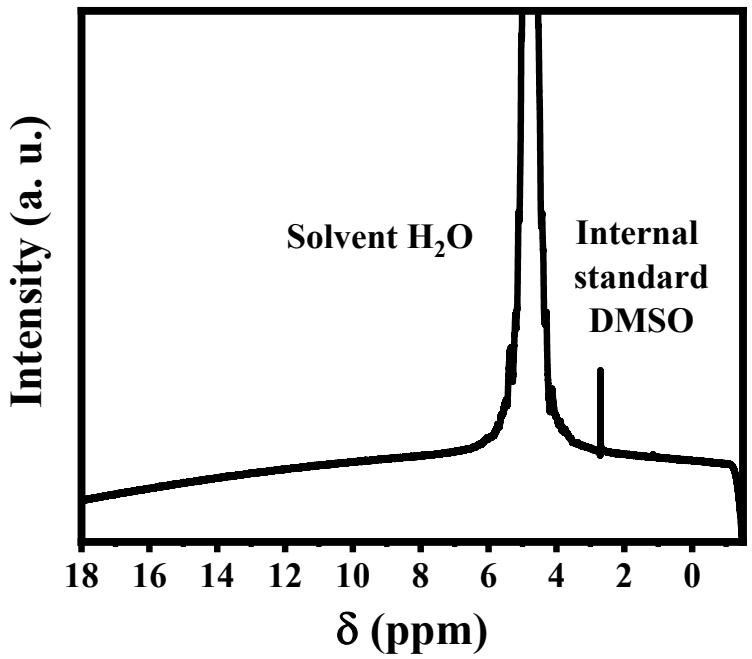

Fig. S5. ^{1}H NMR spectrum of the electrolyte after 1 h electrolysis at −0.72 V *vs*. RHE in 0.5 M $KHCO_3$ solution.

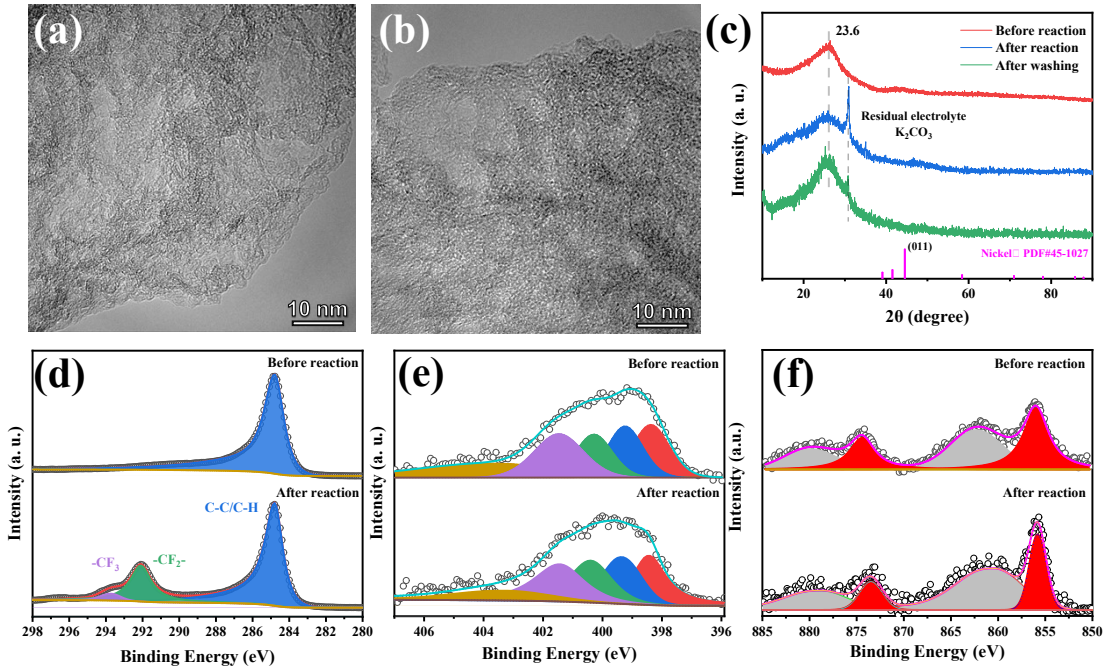

Fig. S6. TEM images of 5Ni@NC-400H (a) before reaction, (b) after reaction; (c) XRD patterns of 5Ni@NC-400H before reaction, after reaction and after washing; (d) XPS spectra of 5Ni@NC-400H before and after reaction in the C 1s region, (e) N 1s region and (f) Ni 2p region.

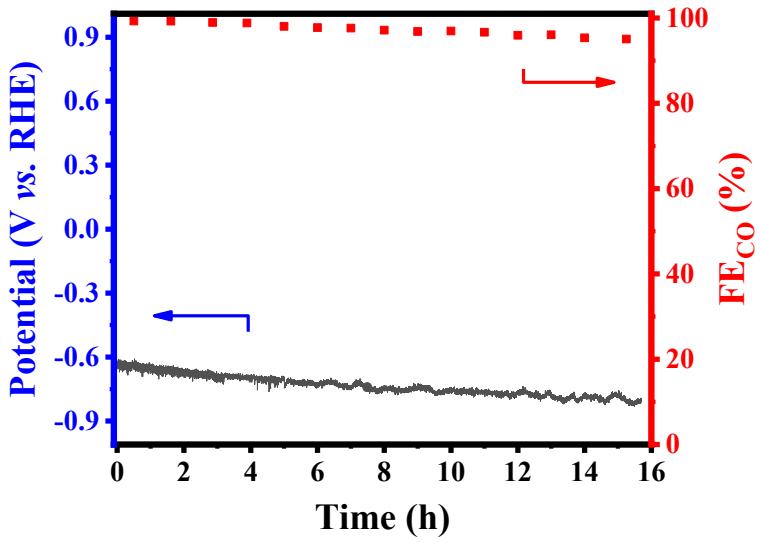

Fig. S7. Long-term stability of 5Ni@NC-400H at −200 mA/cm^2 in 1.0 M KOH electrolyte.

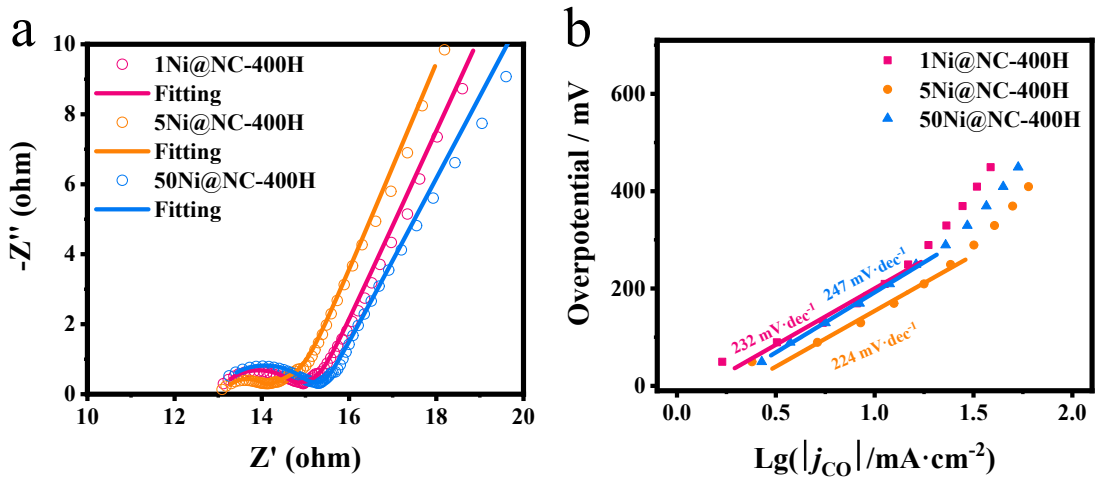

Fig. S8. (a) Electrochemical impedance spectroscopy (EIS) curves and (b) Tafel plots toward CO product with corresponding fitting profiles for xNi@NC-400H catalysts (x = 1, 5 and 50).

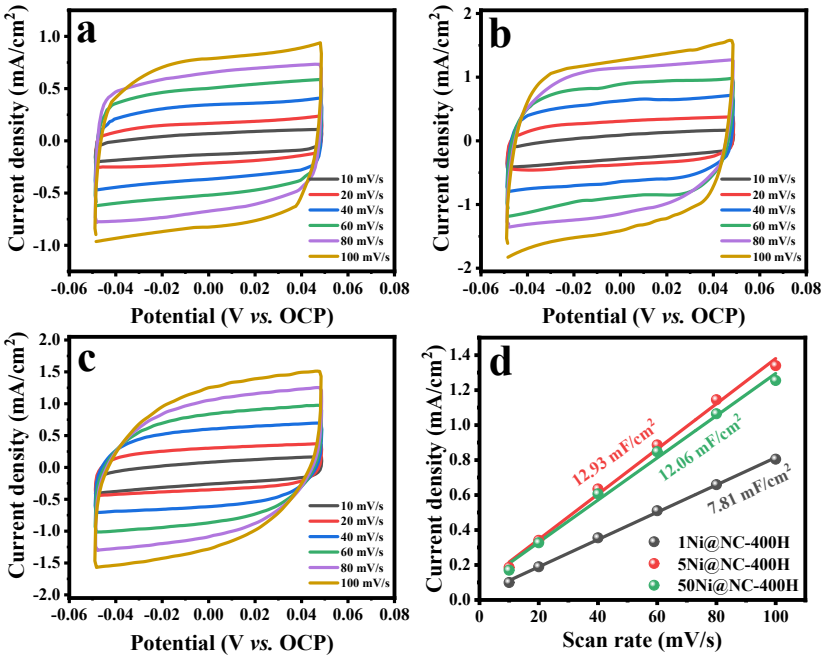

Fig. S9. Cyclic voltammetry (CV) curves obtained at varying scan rates of (a) 1Ni@NC-400H, (b) 5Ni@NC-400H and (c) 50Ni@NC-400H. (d) Charging current density differences (Δj) plotted against scan rates of 1Ni@NC-400H, 5Ni@NC-400H and 50Ni@NC-400H.

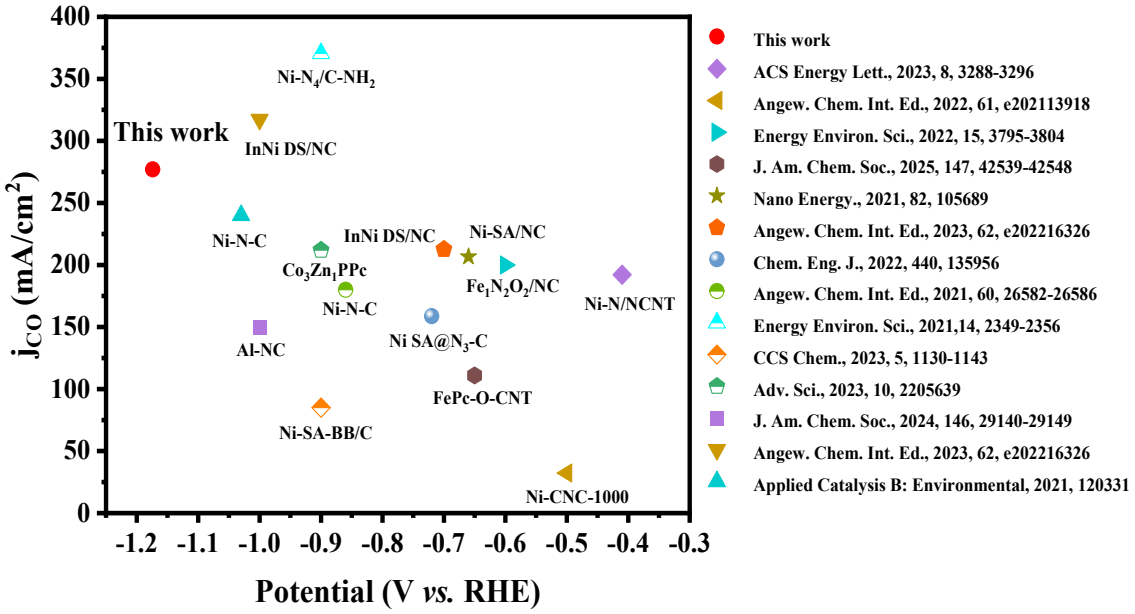

Fig. S10. Comparison of CO partial current density (j_{CO}) values between 5Ni@NC-400H with other reported electrocatalysts evaluated in a flow cell (in 1.0 M KOH electrolyte).

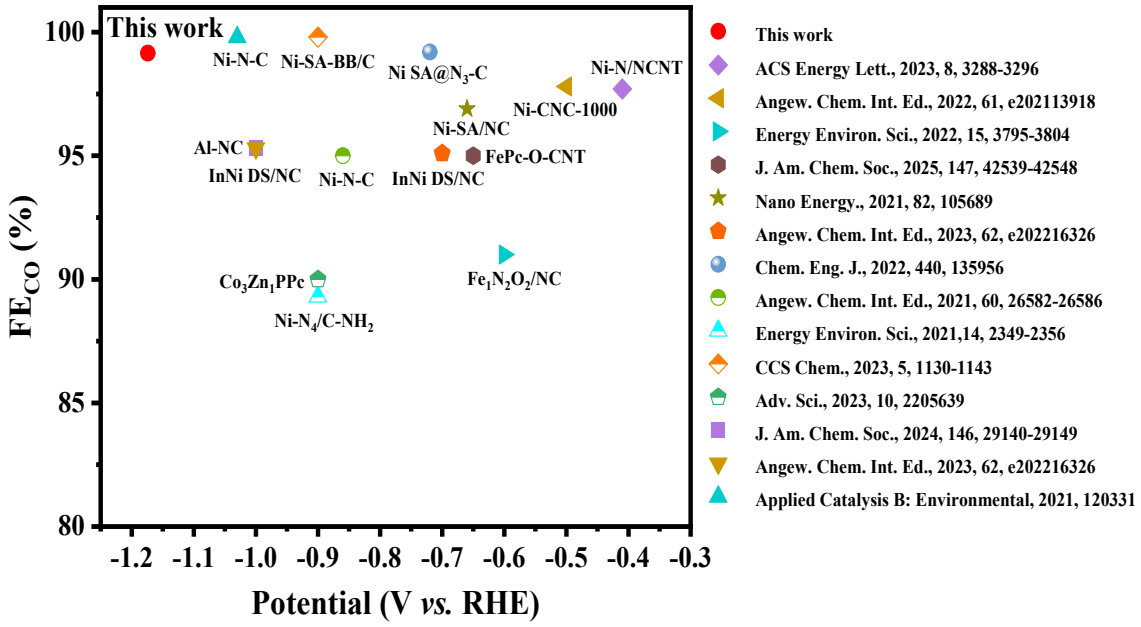

Fig. S11. Comparison of CO Faradaic efficiency (FE_{CO}) values between 5Ni@NC-400H with other reported electrocatalysts evaluated in a flow cell (in 1.0 M KOH electrolyte).

Table S1. Fitting results for N 1s derived from corresponding XPS data.

Sample	Peak	Peak Position	Peak Area (CPS. eV)	Atomic (%)
1Ni@NC-400H	Pyridinic N	398.50	8425.75	33.26
	Ni-N	399.35	2476.09	9.78
	Pyrrolic N	400.48	6602.13	26.10
	Graphitic N	401.88	6433.57	25.46
	Oxidized N	404.58	1362.66	5.40
5Ni@NC-400H	Pyridinic N	398.41	5645.03	30.83
	Ni-N	399.35	3218.05	17.59
	Pyrrolic N	400.38	4697.98	25.70
	Graphitic N	401.46	4098.32	22.43
	Oxidized N	403.26	629.84	3.45
50Ni@NC-400H	Pyridinic N	398.44	7901.35	32.56
	Ni-N	399.33	3440.16	14.19
	Pyrrolic N	400.56	7607.35	31.40
	Graphitic N	401.58	2402.21	9.92
	Oxidized N	403.32	2886.85	11.94

Table S2. Fitting results for Ni 2p derived from corresponding XPS data.

Sample	Peak	Peak Position (eV)	Peak Area (CPS. eV)
1Ni@NC-400H	Ni^{2+} $2p_{3/2}$	855.80	1234.97
	Ni^{2+} $2p_{1/2}$	873.31	639.88
5Ni@NC-400H	Ni^{2+} $2p_{3/2}$	855.70	4444.77
	Ni^{2+} $2p_{1/2}$	873.21	2303.01
50Ni@NC-400H	Ni^{0} $2p_{3/2}$	852.82	1432.89
	Ni^{0} $2p_{1/2}$	870.79	587.55
	Ni^{2+} $2p_{3/2}$	855.72	9155.17
	Ni^{2+} $2p_{1/2}$	873.16	3410.16

Table S3. Results from the analysis of N_2 adsorption-desorption isotherms.

Sample	Surface Area ($m^2 \cdot g^{-1}$)	Pore diameter (nm)
1Ni@NC-400H	862.35	3.506
5Ni@NC-400H	952.06	3.516
50Ni@NC-400H	808.77	3.516

Table S4. The content of Ni loading from ICP-MS test.

Sample	Ni (wt%)
1Ni@NC-400H	0.32
5Ni@NC-400H	1.03
50Ni@NC-400H	5.06

Table S5. Structural parameters of xNi@NC-400H (x =1, 5 and 50) catalysts extracted from the EXAFS fitting.

Sample	Shell	N	R (Å)	σ^2 (Å^2·10^{-3})	ΔE_0 (eV)	R factor
1Ni@NC-400H	Ni-N	4.1	1.94	9.9	5.6	0.011
5Ni@NC-400H	Ni-N	3.4	1.94	9.8	2.7	0.008
	Ni-Ni	0.8	2.47	3.8	-4.7	
50Ni@NC-400H	Ni-Ni	4.6	2.48	6.3	-9.5	0.009

N: coordination numbers; *R*: bond distance; σ^2: Debye-Waller factors; ΔE_0: the inner potential correction; *R factor*: goodness of fit. S_0^2 were set as 0.85/0.89 for Ni-N/Ni-Ni, which were obtained from the experimental EXAFS fit of reference Ni foil/NiPc by fixing coordination numbers as the known crystallographic value and was fixed to all the samples.

Table S6. The comparison of CO_2RR performance with the state-of-the-art Ni-N-C based electrocatalysts.

Catalyst	Electrolyte	Optimal potential (V *vs.* RHE)	FE_{CO} (%)	Stability (h)	FE_{CO} (%) of wide potential window (V *vs.* RHE)	Ref.
5Ni@NC-400H	**0.5 M $KHCO_3$**	**-0.82**	**98.9**	**60**	**-0.62~-1.02 (FE_{CO} 98~98.9)**	**This work**
5Ni@NC-400H	**1 M KOH**	**−0.77**	**99.5**	**16**	**-0.37~-1.17 (FE_{CO} 99~99.5)**	**This work**
Ni-CNC-1000	0.5 M $KHCO_3$	-0.80	96.6	30	-0.6~-1.0 (FE_{CO} 87~96.6)	[8]
Ni_2-N_3C_4	0.5 M $KHCO_3$	-0.88	98.9	30	-0.68~-1.18 (FE_{CO} 90~98.9)	[9]
CA/N-Ni aerogel	0.5 M $KHCO_3$	-0.8	98	12	-0.6~-0.9 (FE_{CO} 96~98)	[10]
Ni-N_4-O/C	0.5 M $KHCO_3$	-0.9	99.2	20	-0.7~-1.0 (FE_{CO} 95~99.2)	[11]
Ni-NC/NHCSs-600	0.5 M $KHCO_3$	-0.87	98.6	14	-0.67~-1.07 (FE_{CO} 90~96)	[12]
Ni-SAC@NC	0.5 M $KHCO_3$	-0.6	95	11	-0.6~-0.9 (FE_{CO} 80~95)	[13]
ZIF-NC-Ni-Fe	0.1 M $KHCO_3$	-0.60	97.8	50	-0.3~-1.0 (FE_{CO} 93~97.8)	[14]
Ni-PCNF	0.1 M $KHCO_3$	-1	94	58	-0.8~-1.2 (FE_{CO} 90~94)	[15]
SA-NiNG-NV	0.5 M $KHCO_3$	-0.70	96.4	20	-0.6~-1.0 (FE_{CO} 82~96.4)	[16]
Co-N-Ni/NPCNSs	0.1 M $KHCO_3$	-0.48	96.4	20	-0.48~-0.68 (FE_{CO} 90~96.4)	[17]
InNi DS/NC	0.5 M $KHCO_3$	-0.70	96.7	10	-0.5~-0.8 (FE_{CO} 90~96.7)	[18]
NiZn-N_6-C	0.5 M $KHCO_3$	-0.8	99	28	-0.5~-1.0 (FE_{CO} 90~99)	[19]
NiO/Ni-N-C-800	0.1 M $KHCO_3$	-1.1	96	10	-0.9~-1.3 (FE_{CO} 93~96)	[20]
NiSAs@3D-INCT	0.5 M $KHCO_3$	-0.86	91.4	12	-0.66~--0.96 (FE_{CO} 80~91.4)	[21]
Ni/Cu-N-C	0.5 M $KHCO_3$	-0.70	97.7	60	-0.5~-1.2 (FE_{CO} 90~97.7)	[22]
Ni-N_4/C-NH_2	0.5 M $KHCO_3$	-0.9	96.2	10	-0.6~-0.9 (FE_{CO} 90~96.2)	[23]
Ni_7/Fe_3-N-C	0.5 M $KHCO_3$	-0.50	98	30	-0.4~-0.7 (FE_{CO} 64~98)	[24]

NiPc-Salen$(Co)_2$-COF	1 M KOH	-0.4	99.8	10	-0.4~-0.8 (FE_{CO} 90~99.8)	[25]
Ni-N-C	1 M KOH	-0.18	~100	15	-0.18~-0.78 (FE_{CO} 95~100)	[26]
Ni-N_3-C	0.5 M $KHCO_3$	-0.65	95.6	10	-0.3~-1.0 (FE_{CO} 80~95.6)	[27]
Ni/Bi-N-C	0.5 M $KHCO_3$	-1.34	~100	10	-0.76~-2.22 (FE_{CO} 90~100)	[28]
M−NiNCx/CNTs	0.1 M $KHCO_3$	-0.7	98	20	-0.6~-0.9 (FE_{CO} 81~98)	[29]
NiSA-N-PGC	0.1 M $KHCO_3$	-0.76	97.2	40	-0.56~-1.06 (FE_{CO} 90~97.2)	[30]

References

[1] G. Kresse, J. Furthmüller, Efficient iterative schemes for ab initio total-energy calculations using a plane-wave basis set, Phys. Rev. B 54(16) (1996) 11169-11186. https://doi.org/10.1103/PhysRevB.54.11169.

[2] G. Kresse, J. Furthmüller, Efficiency of Ab-initio total energy calculations for metals and semiconductors using a plane-wave basis set, Comp. Mater. Sci. 6(1) (1996) 15-50. https://doi.org/https://doi.org/10.1016/0927-0256(96)00008-0.

[3] J.P. Perdew, K. Burke, M. Ernzerhof, Generalized gradient approximation made simple, Phys. Rev. Lett. 77(18) (1996) 3865-3868. https://doi.org/10.1103/PhysRevLett.77.3865.

[4] J.P. Perdew, M. Ernzerhof, K. Burke, Rationale for mixing exact exchange with density functional approximations, J. Chem. Phys. 105(22) (1996) 9982-9985. https://doi.org/10.1063/1.472933.

[5] J.K. Nørskov, J. Rossmeisl, A. Logadottir, L. Lindqvist, J.R. Kitchin, T. Bligaard, H. Jónsson, Origin of the overpotential for oxygen reduction at a fuel-cell cathode, J. Phys. Chem. B 108(46) (2004) 17886-17892. https://doi.org/10.1021/jp047349j.

[6] H.A. Hansen, J.B. Varley, A.A. Peterson, J.K. Nørskov, Understanding trends in the electrocatalytic activity of metals and enzymes for CO_2 reduction to CO, The Journal of Physical Chemistry Letters 4(3) (2013) 388-392. https://doi.org/10.1021/jz3021155.

[7] Y. Li, H. Su, S.H. Chan, Q. Sun, CO_2 electroreduction performance of transition metal dimers supported on graphene: A theoretical study, ACS Catal. 5(11) (2015) 6658-6664. https://doi.org/10.1021/acscatal.5b01165.

[8] X. Cao, L. Zhao, B. Wulan, D. Tan, Q. Chen, J. Ma, J. Zhang, Atomic bridging structure of nickel–nitrogen–carbon for highly efficient electrocatalytic reduction of CO_2, Angew. Chem. Int. Ed. 61(6) (2022) e202113918. https://doi.org/https://doi.org/10.1002/anie.202113918.

[9] Y.-N. Gong, C.-Y. Cao, W.-J. Shi, J.-H. Zhang, J.-H. Deng, T.-B. Lu, D.-C. Zhong, Modulating the electronic structures of dual-atom catalysts via coordination environment engineering for boosting CO_2 electroreduction, Angew. Chem. Int. Ed.

61(51) (2022) e202215187. https://doi.org/https://doi.org/10.1002/anie.202215187.

[10] Y. Zhang, X. Wang, S. Zheng, B. Yang, Z. Li, J. Lu, Q. Zhang, N.M. Adli, L. Lei, G. Wu, Y. Hou, Hierarchical cross-linked carbon aerogels with transition metal-nitrogen sites for highly efficient industrial-level CO_2 electroreduction, Adv. Funct. Mater. 31(45) (2021) 2104377. https://doi.org/https://doi.org/10.1002/adfm.202104377.

[11] S. Wang, P. Zhou, L. Zhou, F. Lv, Y. Sun, Q. Zhang, L. Gu, H. Yang, S. Guo, A unique gas-migration, trapping, and emitting strategy for high-loading single atomic Cd sites for carbon dioxide electroreduction, Nano Lett. 21(10) (2021) 4262-4269. https://doi.org/10.1021/acs.nanolett.1c00432.

[12] S. Gong, W. Wang, R. Lu, M. Zhu, H. Wang, Y. Zhang, J. Xie, C. Wu, J. Liu, M. Li, S. Shao, G. Zhu, X. Lv, Mediating heterogenized nickel phthalocyanine into isolated Ni-N_3 moiety for improving activity and stability of electrocatalytic CO_2 reduction, Appl. Catal. B: Environ. 318 (2022) 121813. https://doi.org/https://doi.org/10.1016/j.apcatb.2022.121813.

[13] Y. Guo, S. Yao, Y. Xue, X. Hu, H. Cui, Z. Zhou, Nickel single-atom catalysts intrinsically promoted by fast pyrolysis for selective electroreduction of CO_2 into CO, Appl. Catal. B: Environ. 304 (2022) 120997. https://doi.org/https://doi.org/10.1016/j.apcatb.2021.120997.

[14] Y. Li, W. Shan, M.J. Zachman, M. Wang, S. Hwang, H. Tabassum, J. Yang, X. Yang, S. Karakalos, Z. Feng, G. Wang, G. Wu, Atomically dispersed dual-metal site catalysts for enhanced CO_2 reduction: Mechanistic insight into active site structures, Angew. Chem. Int. Ed. 61(28) (2022) e202205632. https://doi.org/https://doi.org/10.1002/anie.202205632.

[15] L. Wang, Y. Kong, H. Cai, J. Sun, X. Jiang, X. Li, Q. Hu, H. Yang, C. He, Modulation of d-band electron enables efficient CO_2 electroreduction towards CO on Ni nanoparticles, J. Mater. Chem. A 12(27) (2024) 16403-16409. https://doi.org/10.1039/D4TA02800G.

[16] C. Jia, S. Li, Y. Zhao, R.K. Hocking, W. Ren, X. Chen, Z. Su, W. Yang, Y. Wang, S. Zheng, F. Pan, C. Zhao, Nitrogen vacancy induced coordinative reconstruction of

single-atom Ni catalyst for efficient electrochemical CO_2 reduction, Adv. Funct. Mater. 31(51) (2021) 2107072. https://doi.org/https://doi.org/10.1002/adfm.202107072.

[17] J. Pei, T. Wang, R. Sui, X. Zhang, D. Zhou, F. Qin, X. Zhao, Q. Liu, W. Yan, J. Dong, L. Zheng, A. Li, J. Mao, W. Zhu, W. Chen, Z. Zhuang, N-Bridged Co–N–Ni: new bimetallic sites for promoting electrochemical CO_2 reduction, Energy Environ. Sci. 14(5) (2021) 3019-3028. https://doi.org/10.1039/D0EE03947K.

[18] Z. Fan, R. Luo, Y. Zhang, B. Zhang, P. Zhai, Y. Zhang, C. Wang, J. Gao, W. Zhou, L. Sun, J. Hou, Oxygen-bridged indium-nickel atomic pair as dual-metal active sites enabling synergistic electrocatalytic CO_2 reduction, Angew. Chem. Int. Ed. 62(7) (2023) e202216326. https://doi.org/https://doi.org/10.1002/anie.202216326.

[19] Y. Li, B. Wei, M. Zhu, J. Chen, Q. Jiang, B. Yang, Y. Hou, L. Lei, Z. Li, R. Zhang, Y. Lu, Synergistic effect of atomically dispersed Ni–Zn pair sites for enhanced CO_2 electroreduction, Adv. Mater. 33(41) (2021) 2102212. https://doi.org/https://doi.org/10.1002/adma.202102212.

[20] H. Li, K. Gan, R. Li, H. Huang, J. Niu, Z. Chen, J. Zhou, Y. Yu, J. Qiu, X. He, Highly dispersed NiO clusters induced electron delocalization of Ni-N-C catalysts for enhanced CO_2 electroreduction, Adv. Funct. Mater. 33(1) (2023) 2208622. https://doi.org/https://doi.org/10.1002/adfm.202208622.

[21] W. Xu, Y. Wang, C. Zhang, X. Ma, J. Wu, Y. Liu, B. Lu, H. Zhang, C. Ming, J. Xiang, Insights into the electronic structure coupling effect of dual-metal atomic electrocatalytic platform for efficient clean energy conversion, Chem. Eng. J. 461 (2023) 141911. https://doi.org/https://doi.org/10.1016/j.cej.2023.141911.

[22] J. Zhu, M. Xiao, D. Ren, R. Gao, X. Liu, Z. Zhang, D. Luo, W. Xing, D. Su, A. Yu, Z. Chen, Quasi-covalently coupled Ni–Cu atomic pair for synergistic electroreduction of CO_2, J. Am. Chem. Soc. 144(22) (2022) 9661-9671. https://doi.org/10.1021/jacs.2c00937.

[23] Z. Chen, X. Zhang, W. Liu, M. Jiao, K. Mou, X. Zhang, L. Liu, Amination strategy to boost the CO_2 electroreduction current density of M–N/C single-atom catalysts to the industrial application level, Energy Environ. Sci. 14(4) (2021) 2349-2356. https://doi.org/10.1039/D0EE04052E.

[24] T. Zhang, X. Han, H. Liu, M. Biset-Peiró, X. Zhang, P. Tan, P. Tang, B. Yang, L. Zheng, J.R. Morante, J. Arbiol, Quasi-double-star nickel and iron active sites for high-efficiency carbon dioxide electroreduction, Energy Environ. Sci. 14(9) (2021) 4847-4857. https://doi.org/10.1039/D1EE01592C.

[25] H. Guo, D.-H. Si, H.-J. Zhu, Z.-A. Chen, R. Cao, Y.-B. Huang, Boosting CO_2 electroreduction over a covalent organic framework in the presence of oxygen, Angew. Chem. Int. Ed. 63(14) (2024) e202319472. https://doi.org/https://doi.org/10.1002/anie.202319472.

[26] W. Zhang, C. Zhao, Y. Yang, R. Chen, Y. Wu, J. Dai, Y. Zhang, H. Liu, M. Liu, Highly dispersed atomic-level Ni active sites confined in defects for efficient electrocatalytic reduction of carbon dioxide, J Energy Chem 99 (2024) 1-10. https://doi.org/https://doi.org/10.1016/j.jechem.2024.07.018.

[27] Y. Zhang, L. Jiao, W. Yang, C. Xie, H.-L. Jiang, Rational fabrication of low-coordinate single-atom Ni electrocatalysts by MOFs for highly selective CO_2 reduction, Angew. Chem. Int. Ed. 60(14) (2021) 7607-7611. https://doi.org/https://doi.org/10.1002/anie.202016219.

[28] X. Huang, S. Wu, Z. Xiao, L. Zhi, B. Wang, Atomically dispersed nickel-bismuth dual-atom sites for high rate electrochemical CO_2 reduction, Nano Today 59 (2024) 102477. https://doi.org/https://doi.org/10.1016/j.nantod.2024.102477.

[29] Y. Zhang, T. Sun, P. Zhang, K. Liu, F. Li, L. Xu, Synthesizing MOF-derived NiNC catalyst via surfactant modified strategy for efficient electrocatalytic CO_2 to CO, J. Colloid Interface Sci. 631 (2023) 96-101. https://doi.org/https://doi.org/10.1016/j.jcis.2022.10.146.

[30] M. Huang, B. Deng, X. Zhao, Z. Zhang, F. Li, K. Li, Z. Cui, L. Kong, J. Lu, F. Dong, L. Zhang, P. Chen, Template-sacrificing synthesis of well-defined asymmetrically coordinated single-atom catalysts for highly efficient CO_2 electrocatalytic reduction, ACS Nano 16(2) (2022) 2110-2119. https://doi.org/10.1021/acsnano.1c07746.